

The Formation of Multiple Squall Lines and the Impacts of WSR-88D Radial Winds in a WRF Simulation

HALDUN KARAN, PATRICK J. FITZPATRICK, CHRISTOPHER M. HILL, AND YONGZUO LI

Northern Gulf Institute, Mississippi State University, Stennis Space Center, Mississippi

QINGNONG XIAO AND EUNHA LIM

College of Marine Science, University of South Florida, St. Petersburg, Florida, and National Center for Atmospheric Research, Boulder, Colorado

(Manuscript received 9 January 2009, in final form 4 September 2009)

ABSTRACT

A detailed observational and Weather Research and Forecasting (WRF) model analysis utilizing Weather Surveillance Radar-1988 Doppler (WSR-88D), surface, and upper-air observations, as well as Geostationary Operational Environmental Satellite (GOES) images, shows a chain of events that leads to the formation of two prefrontal squall lines along the western Gulf coast on 29–30 April 2005. An approaching surface cold front (CF) generated an atmospheric bore that propagated along an inversion layer and excited high-frequency, low-level tropospheric gravity waves, initiating a squall line 60 km east of the cold front. This sequence of events manifested itself as low-level convergence ahead of the CF, which was detected by nearby WSR-88D radars. Two WRF model experiments were conducted in which one assimilated conventional observations (CTRL), and another included radar radial winds from nine WSR-88D locations (denoted as RADAR). Better representation of the low-level kinematics in RADAR yielded a distinct convergence line associated with the primary squall line.

The RADAR experiment, as well as observations (such as an 0600 UTC Slidell, Louisiana, sounding), show that the secondary squall line formed ahead of the primary squall line due to high water vapor and warm temperature advection from the Gulf of Mexico that, when combined with a deep dry layer above the atmospheric boundary layer (ABL), destabilized the atmosphere. Concurrently, a lower-tropospheric trough, propagating faster than the surface front, enhanced lifting in the region and instigated the formation of new convection. RADAR forecasted the secondary convection not only in the right place but also at about the right time, while the CTRL experiment completely missed this secondary convection.

1. Introduction

The squall line examined in this study formed in the south-central United States. The system, which was oriented in the northeast–southwest direction, propagated eastward on 29–30 April 2005 across Texas, Missouri, Arkansas, Louisiana, Kentucky, Tennessee, Mississippi, Alabama, and Georgia. The Storm Prediction Center reported large [>1 in. (1 in. = 2.54 cm)] hail, wind damage, and 12 tornadoes, mostly in Mississippi and Alabama. The mesoscale convective system (MCS) later crossed northern Florida

and dissipated over the Atlantic Ocean, 33 h after its formation.

MCSs in the form of squall lines frequently occur in the Great Plains and central United States. Squall lines are most often observed immediately ahead of a cold front (CF), associated with a developing low pressure system. The initiation of deep convection results from convergence and subsequent ascent in the low levels of the atmosphere, typically within the atmospheric boundary layer (ABL). Numerous observational studies show that mesoscale convergence precedes the development of deep convection by several tens of minutes (Ulanski and Garstang 1978; Wilson and Schreiber 1986; Wakimoto and Atkins 1994; Atkins et al. 1995). Convergent boundary zones (CBZs)—such as gust fronts, sea-breeze fronts, drylines, shallow cold fronts, and outflow boundaries—are the primary triggers for deep

Corresponding author address: Haldun Karan, Northern Gulf Institute, Stennis Space Center, Bldg. 1103, Rm. 108, Stennis Space Center, MS 39529.
E-mail: karan@ngi.msstate.edu

convection (Wilhelmson and Chen 1982; Mueller and Carbone 1987; Shapiro et al. 1985; Weckwerth and Wakimoto 1992; Ziegler et al. 1995; Hane et al. 1993; Atkins et al. 1998; Karan and Knupp 2006).

The interaction of CBZs with horizontal convective rolls (HCRs: Xue and Martin 2006; Dailey and Fovell 1999; Fovell 2005; Wakimoto and Kingsmill 1995) and collisions with one another (Intrieri et al. 1990; Kingsmill and Crook 2003) are some triggers for convection. Gravity waves and atmospheric bores (ABs), commonly observed at the inversion level atop the convective boundary layer (CBL), also influence convective initiation (CI; Intrieri et al. 1990; Lac et al. 2002; Koch et al. 2001; Kingsmill and Crook 2003). Investigating a multi-squall-line tornadic event, Locatelli et al. (2002) found the first squall line was initiated by updrafts associated with an undular bore; the bore resulted from the advance of a Pacific cold front into a stable air mass. Fovell et al. (2006) observed a nocturnal squall line caused by gravity wave-induced convection out ahead of the storm system. As concluded from a numerical study by Droegemeier and Wilhelmson (1987) and an observational study by Koch et al. (1991), CI along the CBZ is highly dependent on wind shear and on temperature and water vapor profiles.

Convective lines are also linked to the intensification of thermally direct circulations that transverse a CF. Koch (1984) found that the leading edge of a cloud-free zone was often collocated with initial squall-line development, and that the CF squall line developed as the cloud-free zone behind it reached its maximum extent. Dorian et al. (1988) examined 3 yr of Geostationary Operational Environmental Satellite (GOES) data for squall-line formations associated with secondary circulations transverse surface CFs. They also noted the coexistence of a cloud-free zone behind CFs, stratus clouds at the leading edge of this clear zone, and convective clouds along CFs. Dorian et al. (1988) found thermally direct circulations generated line convection and clear zones, and reported that squall lines formed in 10 out of 15 cases.

To improve the estimate of the initial atmospheric state, the assimilation of radial winds from multiple ground-based Doppler radars into high-resolution mesoscale models has become a focus to deduce convective-scale (spatial scale of 10 km or less, temporal scale of 30 min or less) phenomena. Weather Surveillance Radar-1988 Doppler (WSR-88D) radars are able to delineate CBZs and HCRs in the clear ABL; this capability was utilized by Wilson et al. (1994), and their conclusions are summarized by Weckwerth et al. (1999). Therefore, small-scale kinematic features observed by WSR-88Ds can have a positive impact in the prediction of the location and timing of storm initiation, and the overall evo-

lution of systems. As mesoscale models have gained increasing sophistication, the assimilation of WSR-88D data into numerical models has become more prevalent, allowing for assimilation at high spatial and temporal resolutions, and larger areal coverage. Xiao et al. (2005) have shown significant improvements in short-range, heavy precipitation prediction by assimilating WSR-88D radial winds. Zhao et al. (2006) assimilated multiple radar radial winds to simulate a squall-line system over the eastern United States. They reported a significant improvement in the representation of the three-dimensional wind field and the hydrologic field, but noted a problem with model prediction of storm location. Hu et al. (2006a,b) reported that assimilating reflectivity through a cloud analysis scheme had the greatest impact on the timing and location of two tornadoes, while additionally assimilating radar radial winds strongly influenced the low-level convergence and vorticity, and improved the overall predicted storm structures. Xiao et al. (2008) implemented the Weather Research and Forecasting (WRF) model's three-dimensional variational data assimilation (3DVAR) system using Doppler radial winds and the reflectivity factor Z at the Korean Meteorological Administration, and reported robust improvements in rainfall forecasting.

The purpose of this study is to examine two separate convective initiation mechanisms for the formation of a primary squall line (ahead of a CF) and a secondary squall line (ahead of the primary squall line) over the southeast United States. The impacts of assimilating WSR-88D radial winds on the timing and location of the convection, and the squall-line structure, are also examined to further elucidate the convective triggers. A synoptic overview is presented in section 2. Doppler radar, sounding, surface, and satellite observations are used for a detailed analysis of the primary squall line discussed in section 3, supplemented by a model sensitivity study that assimilates Doppler radial winds. The CI of the secondary squall line is examined in section 4, based on similar data and model analyses. Conclusions are made in section 5.

2. Synoptic features

An overview of the synoptic characteristics is presented for 0000 UTC 30 April in Figs. 1 and 2. The CF location (depicted with connected triangles), and convective cells observed by the Shreveport, Louisiana, radar (KSHV) exceeding 50 dBZ associated with the squall line (diamond shapes), are shown in Fig. 1. Surface high pressure is located over the Texas panhandle, and a pronounced pressure gradient runs from northwest to southeast. Dewpoint temperatures (T_d) across

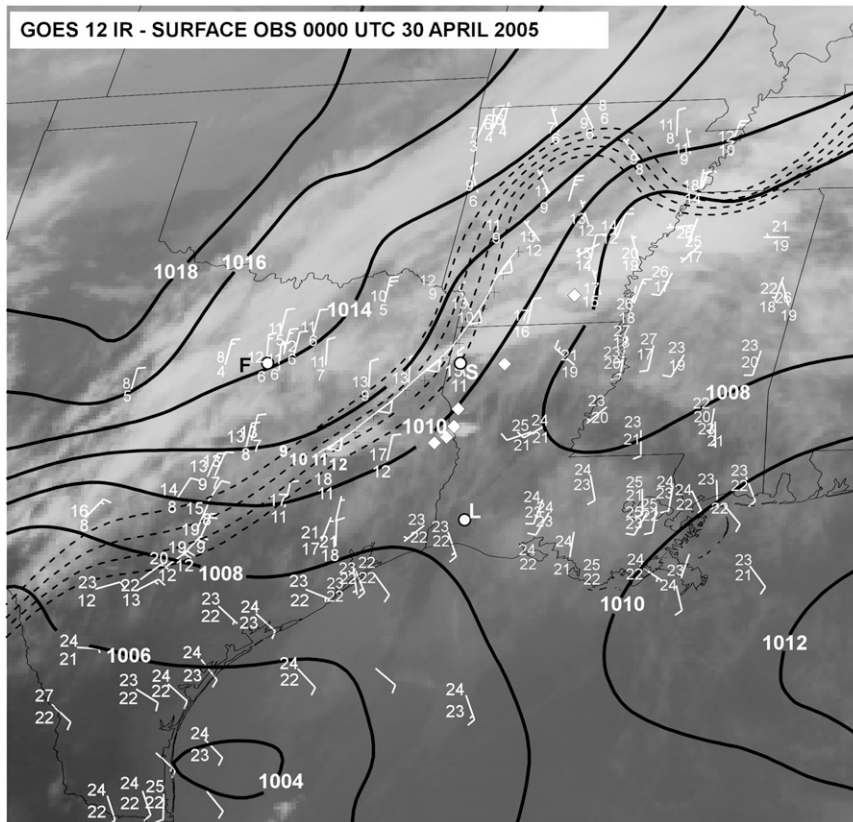


FIG. 1. Surface observations at 0000 UTC (30 April) overlaid on a *GOES-12* infrared image at 2345 UTC 29 Apr 2005. The KFWS, KSHV, and KLCH (Lake Charles, LA) radars are depicted with circles and the letters F, S, and L, respectively. The KSHV radar Z field is used for locations of the intense convective cells (depicted with diamonds) within the developing squall line. KSHV observed radar finelines are used to locate the CF position. The black dashed lines represent the dewpoint temperature contours varying between 9° and 12°C across the cold front. The isobars are depicted with solid lines. Full and half barbs represent 10- and 5-kt winds, respectively.

the CF drop 3°C. Two separate areas of convection are seen in the surface plot (also in Fig. 3a; black and white arrows): CI along the updraft portion of the CF and convection 60–80 km east of the CF. These two convective regions later merge over southern Arkansas. Northerly flow occurs within the squall line and behind the CF. Southerly flow occurs along the Texas–Louisiana–Mississippi coast. This surface flow regime advects warm, moist air toward the cold front. *GOES* visible and infrared imagery, and *WSR-88D* reflectivity data, indicate that once the convective cells were initiated, they quickly propagated northeastward with the strong southwesterly flow aloft.

Convective activity (Figs. 1–3) is observed at the right entrance of the jet stream at 200 mb (not shown). Divergence aloft roughly coincides with the surface convergence ahead of the CF. Behind the surface CF, altostratus and cirrus cloud shields with cloud-top temperatures of -3° to -40°C , respectively, are oriented

in a northeast–southwest direction from central Texas to southeastern Oklahoma, and across Arkansas and Missouri (Fig. 1). This cloud shield coincides with the upstream portion of the short wave at 700–500 mb. Brightness temperatures (Fig. 3a) are relatively higher along this cloud shield than convective cloud tops along the CF and squall line (-30° to -70°C).

A Barnes objective analysis was applied at 850, 700, and 500 mb (Figs. 2a–d). Figures 2c and 2d indicate a short wave over the Texas panhandle and western Texas–New Mexico. Significant and less-pronounced cold-air advection systems over Oklahoma and western Texas, respectively, exist at 850 and 700 mb (Fig. 2a). Gulf coast states and Tennessee experience warm air advection at 850 and 700 mb. A warm front extends from northern Tennessee into northern South Carolina (not shown). The CF location is depicted by fine lines observed by the KSHV radar. Figures 2a and 2c indicate a weak trough at 850 and 700 mb along western

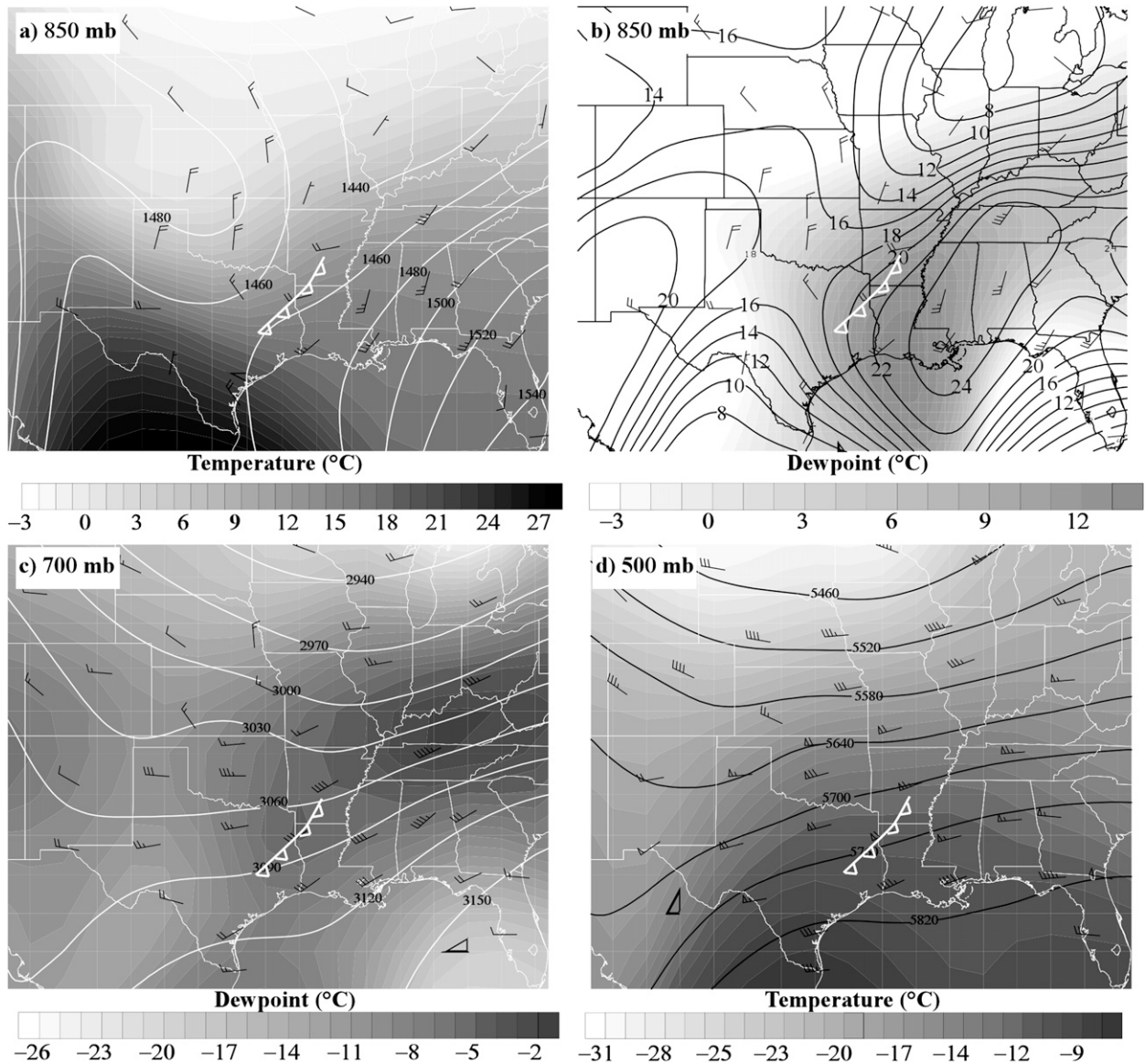


FIG. 2. (a) The 850-mb temperature (shaded) and geopotential heights (solid contours) and (b) the 850-mb dewpoint temperature (shaded) and isotachs (solid contours). (c) Geopotential heights at 700 mb (solid contours) and dewpoint temperature (shaded). (d) Geopotential heights at 500 mb (solid contours) and temperature (shaded) at 0000 UTC 30 Apr 2005.

Louisiana and eastern Texas, and 25–30 kt southwest winds. This weak trough does not appear at 500 mb. Significant moisture advection by southerly flow into southern Louisiana and Mississippi at 850 mb, warm-air advection within the ABL, and cold-air advection at higher altitudes further destabilize the region. The developing instability and secondary squall-line formation will be discussed in section 4.

The squall-line evolution from 0000 to 0900 UTC on 30 April 2005 is shown in Figs. 4a–d. The WSR-88D level III composite Z is chosen to demonstrate the overall squall-line structure. Two distinct convective lines as-

sociated with the CF and the squall line are prominent over eastern Texas and northwestern Louisiana (Fig. 4a). Most of the stratiform-type precipitation associated with the squall line occurs in its northern part. These convective lines merge as the CF moves into northern Louisiana, by 0300 UTC. By 0600 UTC, the line convection becomes one entity, and a new region of convection appears ahead of the primary squall line over southern Louisiana and Mississippi. This region of convection becomes a secondary squall line and merges with the primary squall line by 0900 UTC (Figs. 4c and 4d).

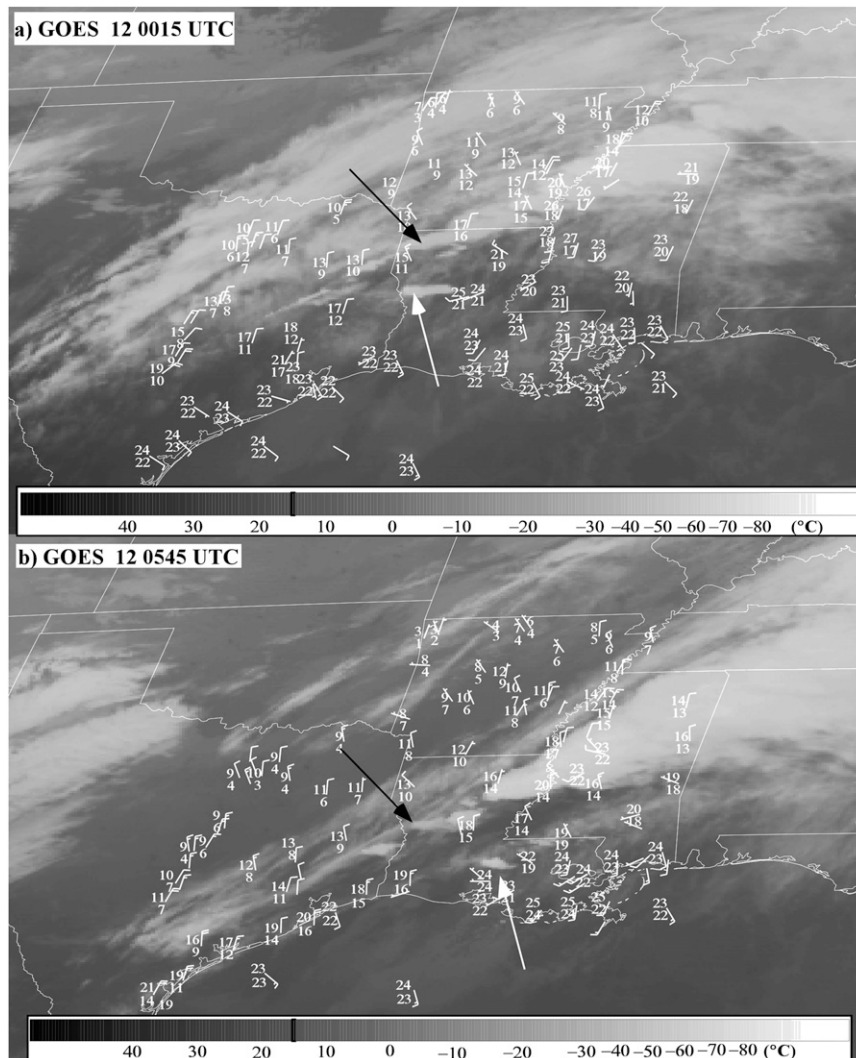


FIG. 3. GOES-12 IR derived brightness temperatures at (a) 0015 and (b) 0545 UTC. The black arrows and the white arrow in (a) depict the line of convection associated with the cold front and initial formation of the primary squall line, respectively. The white arrow in (b) indicates deep cloud development associated with the secondary squall line.

3. Analysis of the primary squall-line formation

A detailed observational analysis of the primary squall-line formation, convective initiation mechanisms, thermodynamic, and kinematic characteristics of the pre-squall-line environment are presented in the following subsections.

a. Cold front and atmospheric bore

The CF was first detected by the Fort Worth, Texas (KFWS), radar as a northeast–southwest-oriented radar fineline around 1444 UTC. The northeastern segment of the CF is depicted by a wide fineline (larger convergence zone) region with reflectivity of 10–24 dBZ, whereas the

southwestern segment is narrower and weakly discernable. As the CF propagated southeastward, it encountered an elevated inversion layer above the ABL, and excited an AB. Atmospheric bores form when gravity-current-type CBZs collapse into a stable, nocturnal inversion layer (Christie et al. 1978; Clarke et al. 1981; Doviak and Ge 1984; Crook 1988; Fulton et al. 1990; Koch et al. 1991; Ralph et al. 1993; Koch and Clark 1999; Knupp 2006). ABs can also form when two density currents (e.g., gust fronts, sea-breeze fronts) collide (Wakimoto and Kingsmill 1995; Simpson 1997; Kingsmill and Crook 2003; Karan and Knupp 2009). Detection of the AB with conventional radars and lidars is possible through Z enhancements. About 2 h before

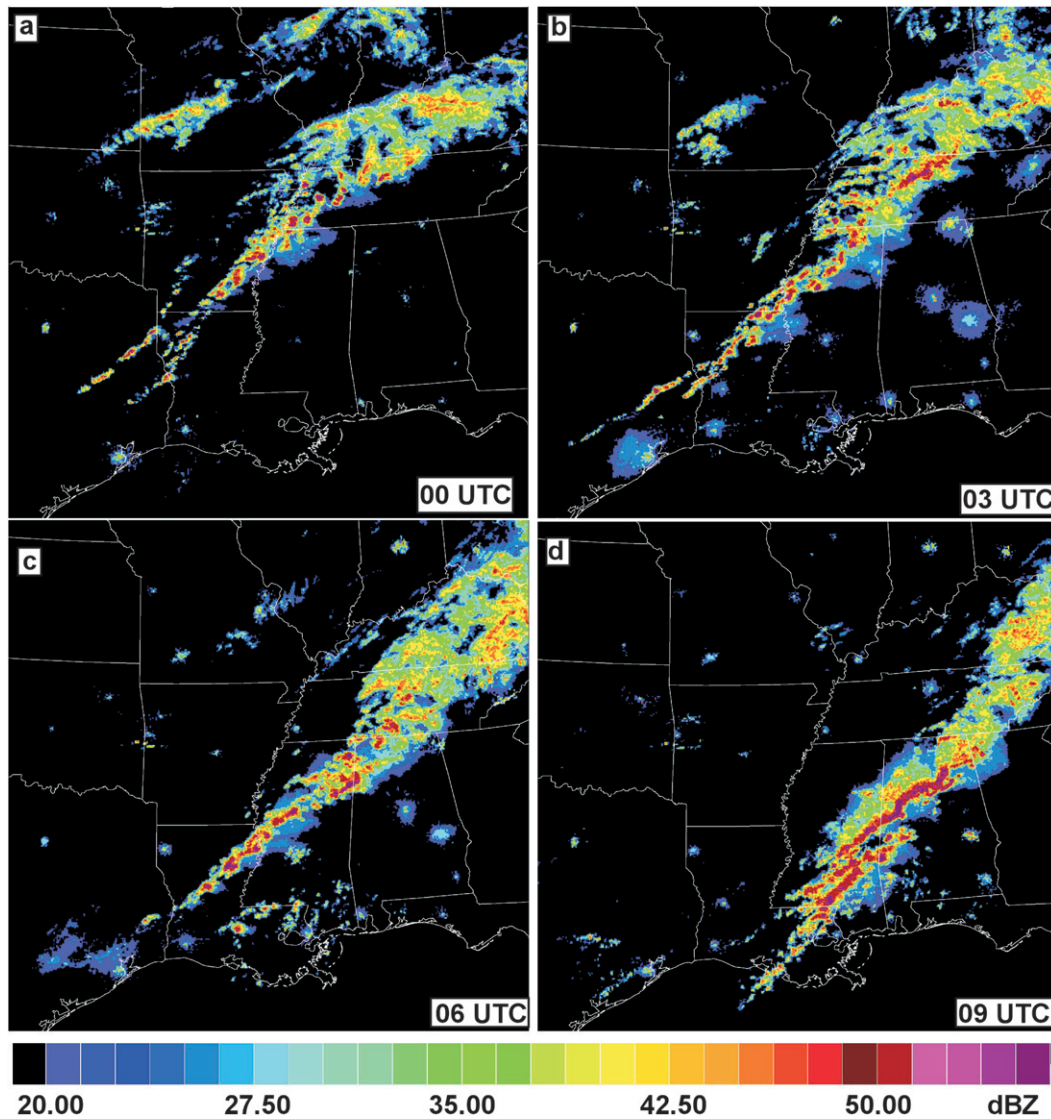


FIG. 4. Composite level III reflectivity factor on 30 Apr 2005 at (a) 0000, (b) 0300, (c) 0600, and (d) 0900 UTC.

the KFWS radar (location indicated with a letter F in Fig. 1) detected the first bore signature, the Fort Worth sounding (Fig. 5) indicated a shallow moist ABL capped with a strong inversion layer at about 1 km AGL. According to the sounding, the ABL was saturated between 0.6 and 1 km. The weak, $2\text{--}3\text{ m s}^{-1}$ southerly low-level wind in the ABL contrasts the southwesterly flow of $\sim 15\text{--}20\text{ m s}^{-1}$ above the ABL, where the atmosphere was dry and strongly stable. The shaded region in the plot represents a prominent stable layer. The virtual potential temperature difference of 8 K across the 0.5-km-deep inversion layer yielded a Brunt-Väisälä frequency N ranging from 2.3 to $2.9 \times 10^{-2}\text{ s}^{-1}$, indicating very strong stability. Conversely, the ABL beneath the inversion layer is weakly stable ($N \sim 6 \times 10^{-3}\text{ s}^{-1}$).

Time series of radar finelines associated with the surface CF and the AB are shown in Fig. 6. The KFWS radar indicated that the AB formed at around 1454 UTC above the northern portion of the CF as a secondary line of enhanced Z. The CF propagated southeastward between 1444 and 1552 UTC (Fig. 6), while the AB ahead of the CF was moving in the same direction between 1454 and 1552 UTC. KFWS reflectivity shown in Fig. 6 is valid at 1533 UTC, at which time the AB is located about 40 km east of the CF. A velocity azimuth display (VAD) analysis (not shown) indicates a wind direction shift from the surface to 1.2 km AGL as the CF passed the KFWS site. The vertical structures of the CF and the AB were reconstructed at approximately 40 min after CF passage over KFWS using the Custom Editing and

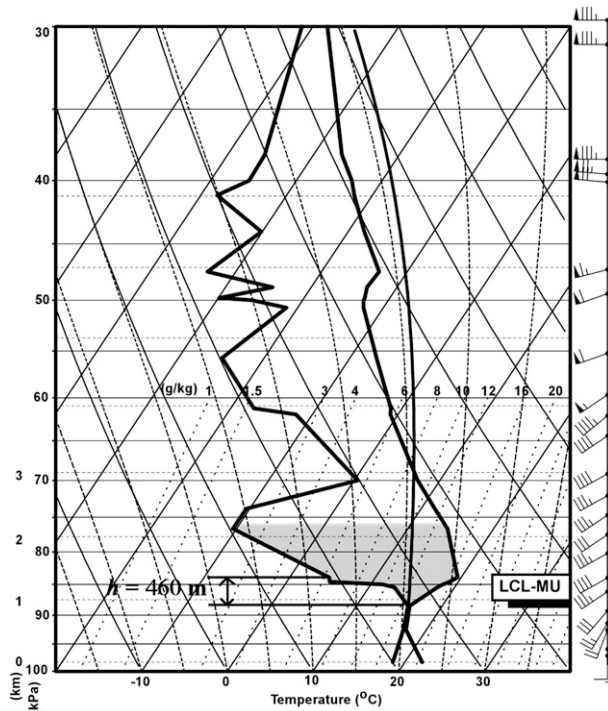


FIG. 5. Fort Worth 1200 UTC 29 Apr 2005 sounding. The most and relatively less stable layers are shaded. The letter “h” depicts the depth of the inversion layer. The virtual potential temperatures at the top and bottom of the inversion layer are 308 and 300 K, respectively. One full barb and the flag represent 10 and 50 kt, respectively.

Display of Reduced Information in Cartesian Space (CEDRIC) software tool. The Z field is interpolated onto a Cartesian grid with 0.25-km spacing in all three directions, and smoothed with the Hanning filter. Missing values are filled with the 3D linear, local least squares method with some predefined constraints. The NW–SE cross section in Fig. 6 at 1612 UTC portrays the vertical structure of the CF and AB in Fig. 7. There are three distinct regions, with high Z values centered at $x = 17.5, 22,$ and 46 km. A narrow region of high Z extends vertically to 0.8 km AGL; this region of relatively large Z is associated with the CF. The second region of enhanced Z was located just above the CF. This secondary, relatively high Z field persisted as the CF propagated southeastward. The wide nature of the anomalous Z region could be explained by the formation of clouds, or by the contraction of insect swarms, induced by updrafts along the CF. As shown earlier, the ABL was well saturated between 0.6 and 1 km AGL, and ambient air can easily be carried to its level of free convection (LFC) with moderate updraft strength. Winds at these altitudes were also very strong ($15\text{--}20\text{ m s}^{-1}$), and may have caused insects to be carried laterally resulting in a wider region for the high Z field. The third region with an enhanced

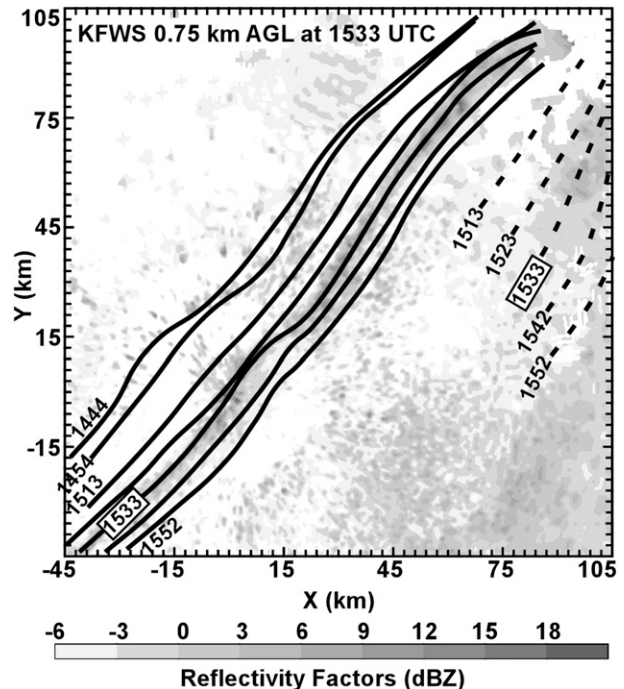


FIG. 6. Fort Worth reflectivity factors at 0.75 km AGL at 1533 UTC 29 Apr 2005. Time series of radar finelines associated with the CF and the AB from 1444 to 1552 UTC are depicted as solid and dashed lines, respectively.

Z field was located 46 km southeast of the radar. Figure 6 shows this third region as radar finelines that are propagating faster than the CF. Isochrone analysis between 1444 and 1552 UTC suggests 5.5 and 14 m s^{-1} propagation speeds of the CF and AB, respectively. Soon after its initiation, the AB propagated about 3 times faster than the CF along the strongly stable inversion layer.

Horizontal displays of Z and radial winds at 1 km AGL (Fig. 8) indicate two distinct finelines 40 km apart. These finelines, propagating toward the southeast, passed over some surface stations in Texas [Lancaster (LAN), Mesquite (MES), and Terrell (TER) airports]; Table 1 shows the surface variable changes as the CF and AB passed over these stations. Typical bore passage is accompanied with a short variation in wind direction, a slight decrease in temperature, and a small pressure increase, depending upon the bore strength. The pressure slightly increased (0.4–0.7 mb) as the AB passed over these stations. Temperature did not change during the AB passage except for TER. At all three stations during the AB passage, T_d decreased by 1°C . LAN and MES reported a wind direction shift during the AB.

The virtual temperature at MES dropped by 4.2 K during the CF passage with a pressure increase of 1.9 mb. Assuming no vertical density differences between the environment and the cold air within the CF (i.e., virtual

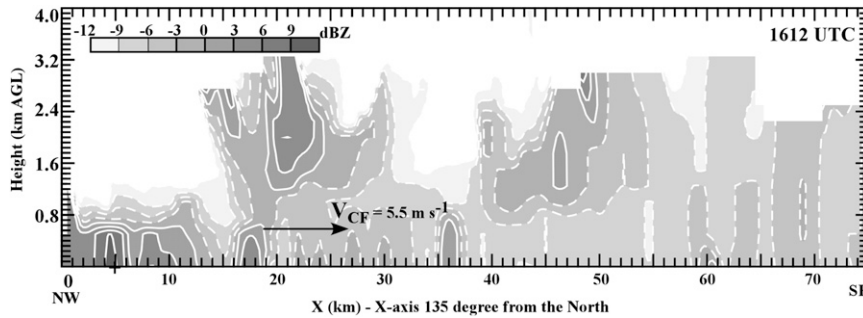


FIG. 7. Radar reflectivity factor across the NW–SE cross section of the CF at 1612 UTC 29 April 2005; V_{CF} is the propagation speed of the CF and negative values are depicted with dashed contours.

temperature reduction across the boundary does not change with height), the mean depth of a gravity current d_o can be derived from the hydrostatic assumption (Koch et al. 1991) as

$$d_o = \frac{T_{vc} \Delta p}{\rho_w g [(p_c/p_w) T_{vw} - T_{vc}]}, \quad (1)$$

where the c and w subscripts denote values within the cold and ambient air, respectively. In addition, T_v , p , ρ , and g are the virtual temperature, pressure, density, and acceleration due to gravity, respectively. Substitutions of MES observations yield a d_o of about 1 km, which closely agrees with the observed 0.8-km-deep CF seen in Fig. 7.

Rottman and Simpson (1989) conducted laboratory experiments showing that gravity currents can produce internal bores on the interface of a two-layer fluid. They

hypothesized that bore generation by gravity currents is dependent on the ratio of the gravity current depth to the stable-layer depth. In this study, the morning inversion layer was gradually elevated above a relatively neutral layer, and was about 0.5 km deep. The internal Froude number F_r (ratio of the inertial force to the force of gravity) is about 0.4, small for typical gravity currents. Kingsmill and Crook (2003) found that F_r varied between 0.7 and 1.4 for gust fronts, and 0.5 and 1.0 for sea-breeze fronts. Shallow cold fronts are also shown to be dynamically similar to gravity currents (Karan and Knupp 2006). The sounding (Fig. 5) suggests a shallow neutral ABL and a deep, dry stable layer above. Therefore, the total depth h_o of the stable layer, including the weakly stable ABL, is about 1.5 km. The ratio of d_o/h_o then becomes 0.8. The F_r and the ratio, d_o/h_o , falls within the range of partially blocked-type flow regimes (Fig. 2 in

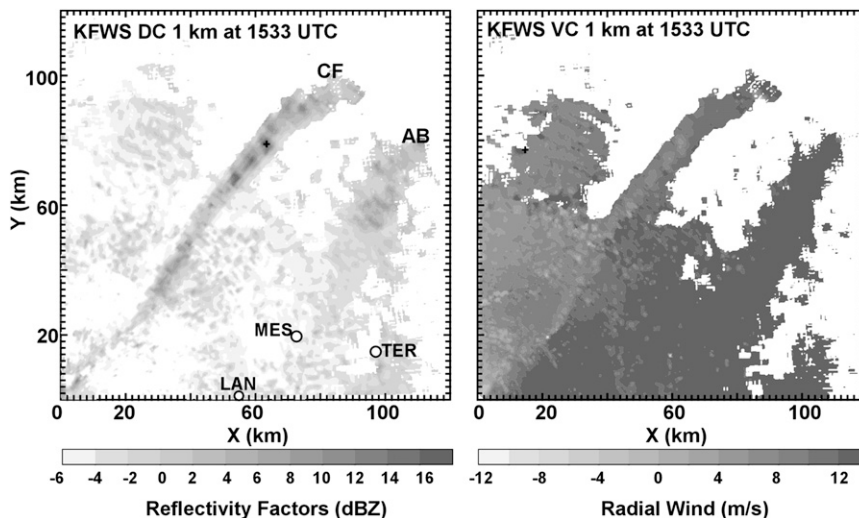


FIG. 8. Fort Worth WSR-88D radar (left) reflectivity factor and (right) radial winds at 1 km AGL at 1533 UTC 29 Apr 2005. CF and AB indicate the cold front and atmospheric bore, respectively. The radar is located at (0, 0) position. The Lancaster (LAN), Mesquite (MES), and Terrel (TER) airports are denoted by circles.

TABLE 1. Surface variable changes during the CF and AB passages. The locations of these surface stations relative to the CF and AB are shown in Fig. 8.

	ΔT ($^{\circ}\text{C}$)		ΔT_d ($^{\circ}\text{C}$)		ΔV (m s^{-1})		Δ direction ($^{\circ}$)		ΔP (mb)	
	AB	CF	AB	CF	AB	CF	AB	CF	AB	CF
LAN	—	-2	-1	-1	2.9	—	20	—	0.3	1
MES	—	-2	-1	—	1.8	1	10	—	0.4	1.9
TER	1.1	-2.2	-1.1	-1.1	2.3	1.2	—	—	0.7	2.4

Rottman and Simpson 1989). This type of flow regime, in which h_1/h_o is between 1 and 2, produces a smooth undular flow pattern. Here, h_1 represents the mean bore depth. An approximate depth of the AB (Fig. 7) is about 2.0 km. The bore strength in this case is about 1.3, which suggests that the disturbance at the top of the CF was associated with an internal undular bore.

As mentioned earlier, the observed propagation speed of the bore for the time period between 1454 and 1552 UTC was about 14 m s^{-1} . Since F_r can also be defined as the ratio of the propagation speed of the gravity current to the phase speed of the gravity wave (Rottman and Simpson 1989), the values of $F_r = 0.4$ and $C_{gc} = 5.5 \text{ m s}^{-1}$ yield a bore speed of 13.8 m s^{-1} , very close to the observed propagation speed.

b. ABL properties during the squall-line formation and gravity waves

Close inspection of Z reveals that as the AB propagated toward the southeast, it excited gravity waves that eventually initiated convection ahead of the CF. In this case, the gravity waves are shown to be the cause for

the squall-line formation that occurred about 100 km ahead (east) of the CF. KSHV observed an intermittent but gradual increase in Z in the form of northeast-southwest-oriented bands to its west from 1800 to 2000 UTC. A sequence of Z during this period indicates that an AB moving ahead of the CF excited gravity waves. A snapshot of these bands at 0.75 km AGL is shown in Fig. 9a. Signatures of the gravity waves are associated with enhancements in Z from 8 to 15 dBZ between 1800 and 1900 UTC, and from 25 to 30 dBZ for 1900 and 2000 UTC. Values of 25–30 dBZ are typically associated with cloud formation and ≥ 30 dBZ with CI. At 2030 UTC, the CF was located 80 km west of the gravity waves, with banded features of Z (~ 30 –35 dBZ) west and north of the radar.

Figure 9a displays wave activity oriented NE to SW mainly west of the KSHV radar. Large Z values of 20–23 dBZ (mostly due to clear-air returns and/or Bragg scattering) are observed along the wave crests at 1930 UTC, while the CF was located 150 km northwest of the radar site (not shown in the figure). The waves propagated southeastward while the convection expanded northward and intensified over time. The convection ahead of and along the CF at 2200 UTC is shown in Fig. 9b. The CF, at this time, is located 60 km west of the convective activity, which later becomes the primary squall line. Convective cells with values of 35–50 dBZ are also depicted along and ahead of the CF.

c. Characteristics of the environment and CI

The Shreveport sounding at 1800 UTC (Fig. 10) shows strong southwesterly (30–40 kt) uniform flow within the

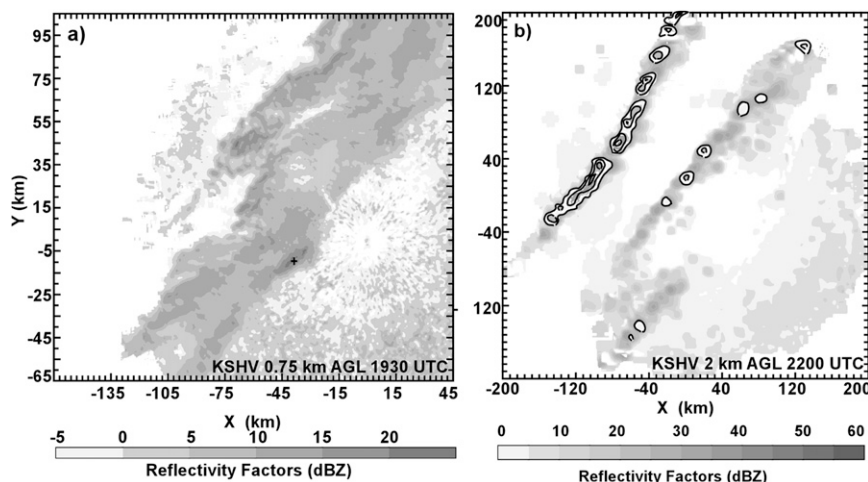


FIG. 9. KSHV WSR-88D reflectivity factor (a) at 0.75 km AGL at 1930 UTC and (b) at 2 km at 2200 UTC. Values less than -5 dBZ are not shown in (a). The Z values larger than 35 dBZ are depicted with contouring in (b). CF depicts the location of the cold front. The black circle depicts the KSHV radar location.

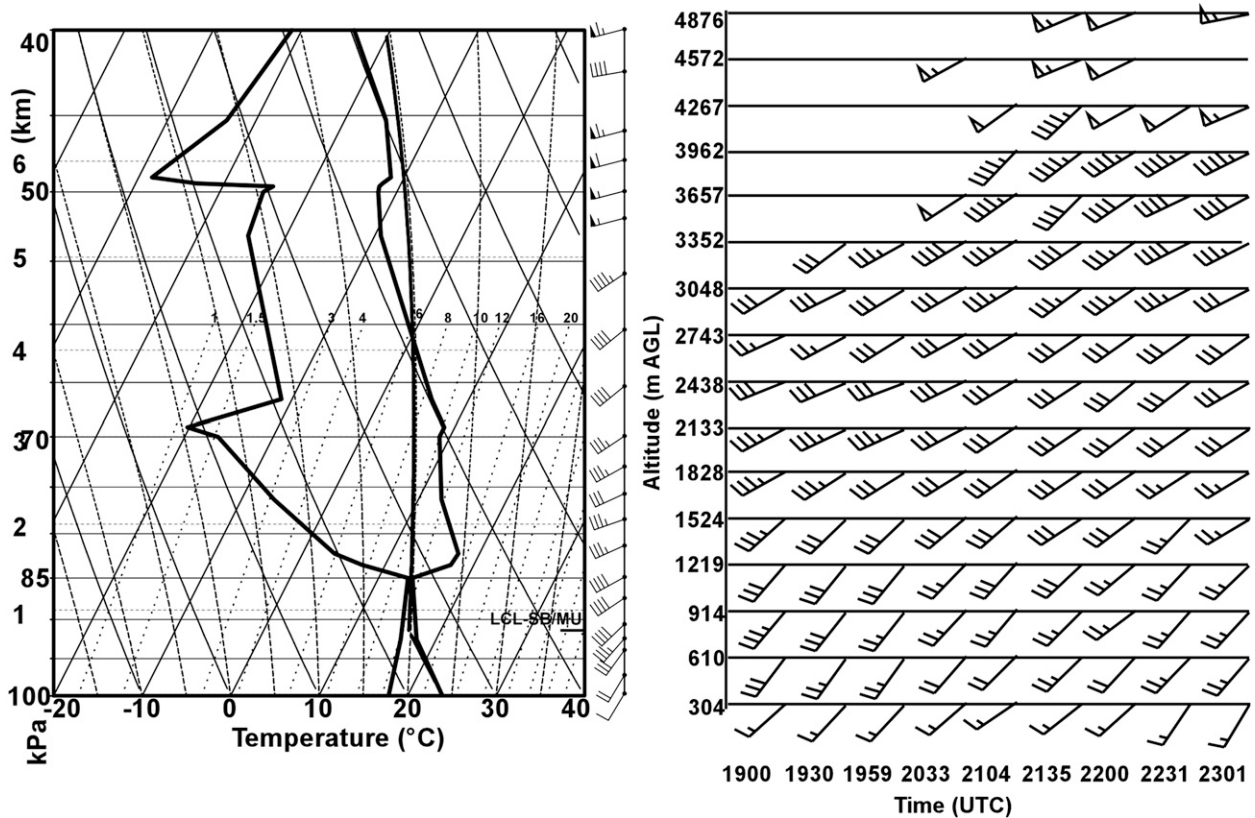


FIG. 10. (left) Shreveport 1800 UTC sounding on 29 Apr 2005. (right) Time series of VAD at KSHV. Winds with one full barb represent 10 kt. See the letter S in Fig. 1 for the location.

ABL. The upper-tropospheric flow was westerly at 60–70 kt. The VAD time series analysis from the KSHV radar starting 1900 UTC for every 30 min is also shown. The ABL had strong southwesterly flow from 0.6 to 3 km AGL, with shear values at the 0–3- and 0–6-km layers of $4 \times 10^{-3} \text{ s}^{-1}$. The strongest shear was about $1 \times 10^{-2} \text{ s}^{-1}$. Like the 1200 UTC Fort Worth sounding (Fig. 5), the environment between 850 and 700 mb was significantly dry. The sounding also indicated very low convective available potential energy ($\text{CAPE} < 200 \text{ J kg}^{-1}$) and high convective inhibition ($\text{CIN} > 250 \text{ J kg}^{-1}$). The existence of clouds from 0.8 km (0.6 km beneath the ABL top) is also suggested. Figure 11 shows an inversion layer above 1.4 km where virtual potential temperature θ_v increases sharply. Using an average θ_v (304.2 K) within the stable layer, and a θ_v variation (7 K) across the layer yields an average N of $2.8 \times 10^{-2} \text{ s}^{-1}$. Waves can be trapped under these conditions where a strong deep stable layer exists above a weakly stable atmosphere. The impacts of ambient stratification on the density current structure, evolution, and propagation have been investigated through theory, laboratory experiments, observations, and numerical models (e.g., Benjamin 1968; Drogemeier and Wilhelmson

1987; Simpson 1997; Xu 1992; Xu and Moncrieff 1994; Liu and Moncrieff 1996; Xue et al. 1997; Moncrieff and Liu 1999). Liu and Moncrieff (2000), using a two-dimensional nonhydrostatic model, investigated how

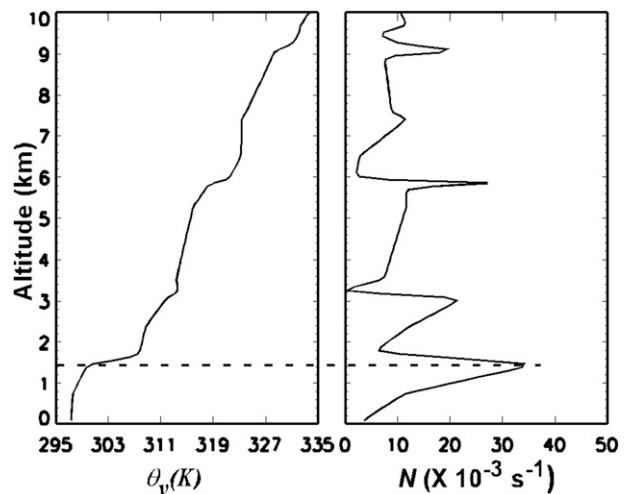


FIG. 11. Vertical profiles of (left) virtual potential temperature and (right) Brunt-Väisälä frequency from the 1800 UTC Shreveport sounding. The dashed line depicts the level of the inversion base.

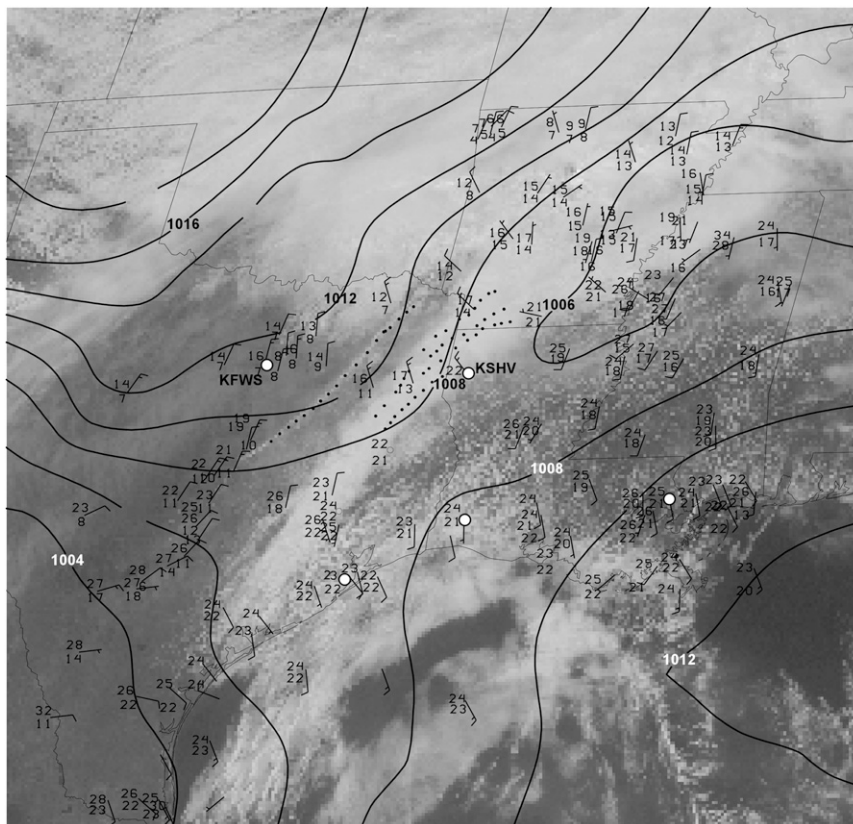


FIG. 12. Surface observations at 2000 UTC overlaid on a GOES visible image at 1945 UTC 29 Apr 2005. Solid contours are the isobars. Full barbs represent 10-kt winds. White circles depict radar stations for Fort Worth, KSHV, and Galveston in TX, and Lake Charles and Slidell in LA. KFWS and KSHV depict the locations of the Fort Worth and Shreveport radars. The westernmost dotted line is the CF location. The dotted lines east of the CF depict the gravity waves.

stratification strength and its distribution regulated the behavior of density currents by employing different sets of N . As the sounding suggested (Fig. 10), the ABL ahead of the approaching CF was shallow and neutral. A deep, stable atmospheric layer above the ABL existed (Figs. 10 and 11). A study done by Liu and Moncrieff (2000) showed a multihead structure, with several wavelike disturbances propagating upstream of the leading edge of the density current under intermediate and strong low-level stratification ($N = 12 \times 10^{-3} \text{ s}^{-1}$ and $18 \times 10^{-3} \text{ s}^{-1}$) for “nocturnal conditions” (Figs. 5 and 6 in Liu and Moncrieff 2000). For the strongest stratification case, leading multiple solitary-wave-like structures propagated faster and decoupled the density current head. The strong stratification above the ABL acts like an obstacle, generating gravity waves that reach far ahead of the density current, and to higher altitudes. The neutral condition within the ABL, and a deep, upper-level stratification ($N = 28 \times 10^{-3} \text{ s}^{-1}$) for the case investigated in this study, verifies that the gravity wave

excitation was a consequence of the interaction between the CF and the ambient air. Based on the profile of N (Fig. 11), calculations suggest a high-frequency period of 5 min for waves forming at the ABL top. Based on KSHV data, wavelengths of the gravity waves were about 10–15 km.

The CF at 2000 UTC (Fig. 12) is accompanied with a relatively clear zone 60–80 km to its east. Behind the CF, another clear (cloud-free region) zone is also evident. Surface observations indicate reductions of about 3°C in T and 6°C in T_d between the cold air of the CF and the air within the band of the stratocumulus region ahead of the CF. This stratocumulus cloud shield will later become the region of intense convection. The variations of T and T_d are even greater in the southern portion of the CF. The flow below the stratus cloud region was northerly, like the flow behind the CF. Ahead of this cloudy region, southerly surface winds bring moisture and warmer temperatures to the region. Figure 12 also depicts the location of the gravity wave

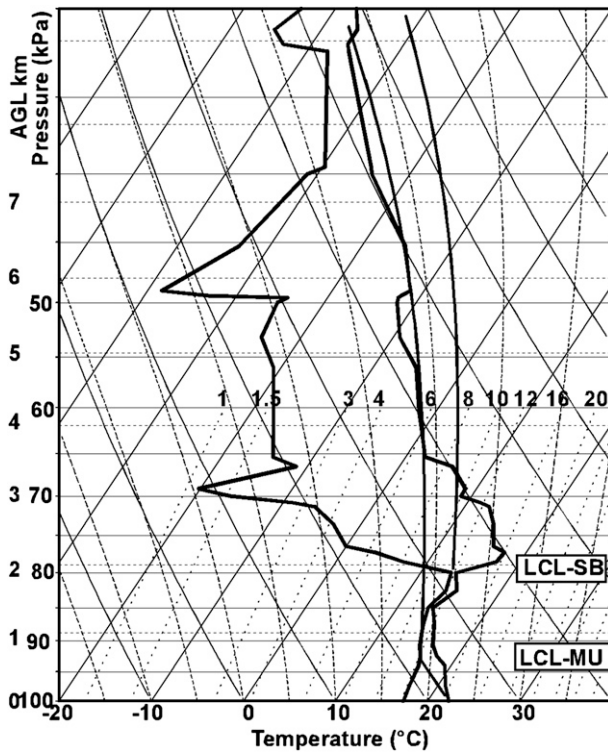


FIG. 13. Modified 1800 UTC Shreveport sounding by lifting the layer of 875–763 mb.

disturbances with bands of dotted line over northwestern Louisiana and south Arkansas. Relative maximum values of Z observed by the KSHV radar were used to determine the locations. As shown earlier, the sounding at 1800 UTC indicates the existence of clouds beneath the ABL top. Figure 12 verifies a stratocumulus cloud shield ahead of the CF, extending from the southern coast of Texas into southern Arkansas. The KSHV Z field at 2200 UTC indicates that the convection occurred within this stratocumulus region (Fig. 9b).

The Shreveport sounding was modified by lifting a part of the layer believed to be affected by the AB passage (Fig. 13). As discussed earlier, an AB occupied the layer between 1.2 and 2.4 km. This layer corresponds to 875–763 mb (~1219–2377 m AGL layer). Two 50-mb layers (875–825 and 825–775 mb) were averaged and the layer was lifted. Figure 13 shows the AB’s impact on the thermodynamic environment based on the modified sounding. A deep moist layer exists to 800 mb, capped by a strong inversion. There is still significant dry and stable layer above that level. The most unstable CAPE increases from 200 to 1241 J kg⁻¹ while the CIN decreases to 130 J kg⁻¹. Recall that the layer was only lifted 50 mb (~500 m) while the AB was 112 mb deep. The passage of the AB was strong enough to bring ABL air parcels to the LFC.

This sequence of events manifested itself as low-level convergence ahead of the CF. The kinematics can be detected by WSR-88D radars and assimilated to improve model prediction of squall-line events. Model diagnostics of kinematics based on the assimilation of Doppler radial winds are discussed in the next subsection.

d. Model diagnostic of primary squall-line kinematics

The WRF model and its 3DVAR system (Skamarock et al. 2005) are used to study the squall-line events. The North American Mesoscale (NAM) model analysis provides the initial and boundary conditions. Background error covariances are determined by the National Meteorological Center [NMC, now known as the National Centers for Environmental Prediction (NCEP)] method (Parrish and Derber 1992) using a 12-h cycling mode during 1–15 April to generate model background errors as described by Barker et al. (2004) and Skamarock et al. (2005).¹ The WRF domain covers the southeast United States and northern Gulf of Mexico with a grid spacing of 4 km distributed over 350 × 350 horizontal grid points and 35 vertical points, centered over Mississippi. Standard observations from the Global Telecommunication System (GTS), and the U.S. Geological Survey’s (USGS) Soil Climate Analysis Network (SCAN) are used in 3DVAR as a control experiment (hereafter CTRL). Radial velocities from nine WSR-88D radars (see Fig. 14 for locations), plus the GTS and SCAN observations, are assimilated in a second experiment (denoted as RADAR). The WSR-88D radial winds are edited, unfolded, and quality checked. The physics options in this study include the WRF single-moment five-class microphysics scheme (WSM-5; Lim and Hong 2005); the Yonsei University (YSU) boundary layer parameterization, which accounts for local and nonlocal mixing (Hong and Noh 2006); the Dudhia shortwave parameterization (Dudhia 1989); and the Rapid Radiative Transfer Model (RRTM) longwave parameterization (Mlawer et al. 1997). Cumulus parameterization was turned off in the high-resolution inner grid. The squall-line case study is assimilated in a 3-h cycling mode from 1800 UTC 29 April to 0000 UTC 30 April, whereupon the simulation begins.

¹ Background errors were also generated at 6-h time intervals (total of 60 forecasts). The innovations or increment differences with RADAR and GTS were found to be very small between the 12- and 6-h time intervals.

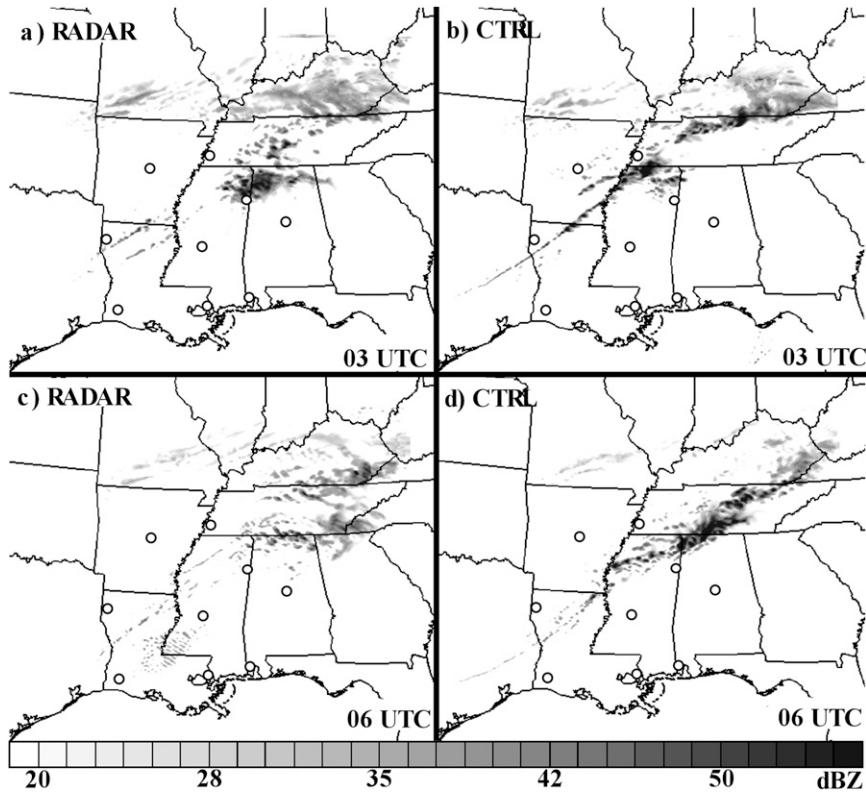


FIG. 14. (a),(c) RADAR and (b),(d) CTRL composite reflectivity factors at forecast hours 3 and 6 in the WRF simulation. Locations of the WSR-88D radar sites used in 3DVAR are depicted as circles.

The WRF composite Z at our 0300 UTC forecast hour (Figs. 14a–d) reveals important differences between the two WRF experiments. The CTRL experiment simulated more pronounced convection along the CF, resembling the 0300 UTC observations. However, RADAR clearly depicts two regions of convection:

along the CF and along the primary squall line. The primary squall line observed over west-central Louisiana at 0300 UTC (Fig. 4b) matches well with the convection simulated in the RADAR experiment. The alongfront convection simulated in the RADAR experiment is weaker than the convection in the CTRL

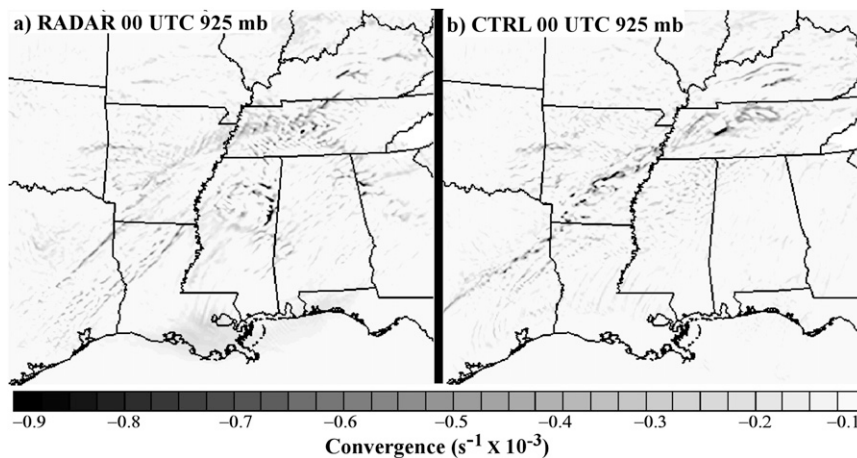


FIG. 15. Convergence fields at the 925-mb level at the 0000 UTC 30 Apr 2005 model initial time for the two experiments.

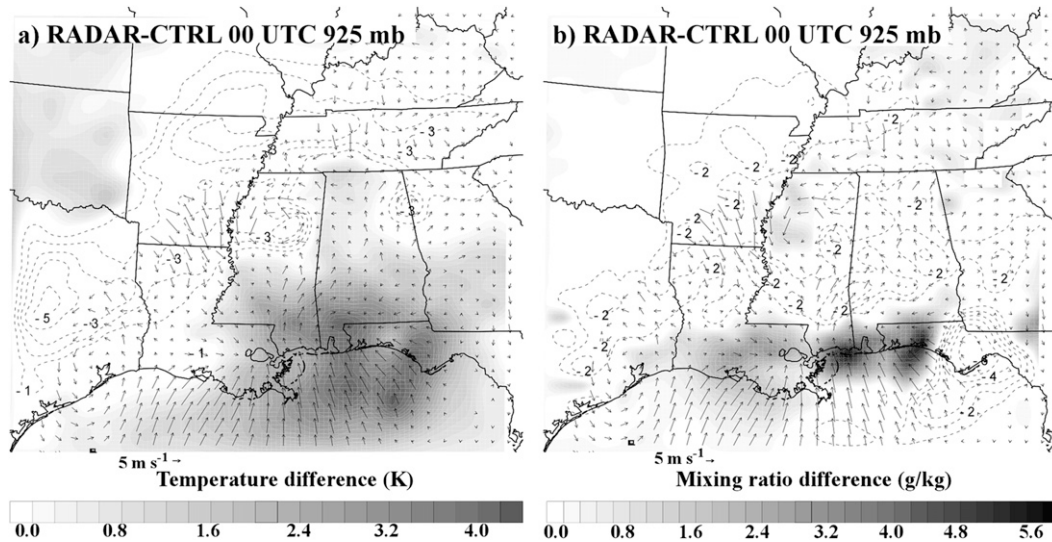


FIG. 16. Differences in wind and (a) temperature and (b) mixing ratio between the RADAR and CTRL experiments. Only the wind differences on the east of the cold front are plotted.

experiment. However, it demonstrates better structural similarities against the observations, especially over Tennessee and Kentucky.

To determine the impacts of radial winds on model initialization, $\mathbf{V} \cdot \mathbf{V}$ is computed at 925, 850, 700, and 500 mb (Fig. 15). This analysis focuses on $\mathbf{V} \cdot \mathbf{V}$ along the CF and the primary squall line. CTRL exhibits greater convergence along the surface CF than RADAR. For instance, convergence at 925, 850, and 700 mb along the CF is 2 times greater than RADAR (Fig. 15). At 500 mb (not shown), the maximum convergence along the cold front for CTRL is 7 times greater than the maximum value for RADAR. Overall, the layer-averaged convergences at 925–850 and 925–700 mb are 2 times greater for the CTRL experiment. The simulations with assimilated radial winds capture the location and structure of the primary squall line. Structural resemblance of the squall line between the observations (Fig. 4a) and RADAR is acceptable. A reasonably accurate simulation is important for the subsequent analysis of the secondary squall line discussed in the next section. Figure 15a shows a secondary line of convergence extending from eastern Texas into Louisiana, and northern Mississippi, which will be analyzed next.

4. Analysis of the secondary squall-line formation

The WRF simulation suggests a different set of circumstances for CI of the secondary squall line. The following subsections discuss the influence of a low-level trough and developing instability. As will be seen, capturing the proper wind regime is important to understanding the sequence of events for the secondary squall line.

a. Thermodynamic setup for secondary squall-line development

At the model initial time, surface thermodynamic and kinematic characteristics are shown in Figs. 16 and 17. RADAR starts with warmer temperatures ($\sim 2\text{--}4\text{ K}$) and higher water vapor ($\sim 1\text{--}6\text{ g kg}^{-1}$) over southern portions of Louisiana, Mississippi, and Alabama. Figure 16 also indicates that CTRL is initialized with colder and drier air behind the cold front (shown as dashed contours). Wind vector differences between the two experiments reveal $5\text{--}10\text{ m s}^{-1}$ greater southerly winds flowing into southern Louisiana, Mississippi, and Alabama. The vertical structures of the temperature and water vapor at model initialization (not shown) indicate that the coastal differences between the two experiments exist only at and below 850 mb for the temperature and 700 mb for the water vapor fields, possibly because more radial wind observations used in 3DVAR originated at the lowest radar elevation angles. Between the two experiments, RADAR starts the simulation with higher temperature and water vapor advection over the southern states ($3\text{--}5\text{ K s}^{-1} \times 10^{-4}$ and $3\text{--}5\text{ g kg}^{-1}\text{ s}^{-1} \times 10^{-4}$ more; Fig. 17). This yields temperature and water vapor increases of more than 1 K and $1\text{--}2\text{ (g kg}^{-1}\text{) h}^{-1}$ over the region. The RADAR 0300 UTC forecast (not shown) indicates about 2–5 K warmer temperatures over the northern Gulf of Mexico and along the Gulf coast of Louisiana, Mississippi, Alabama, and central Mississippi and Alabama. At the same forecast hour, RADAR also produces $1\text{--}6\text{ g kg}^{-1}$ more water vapor over the southern portions of the southern states (not shown). RADAR suggests a secondary line of convergence over

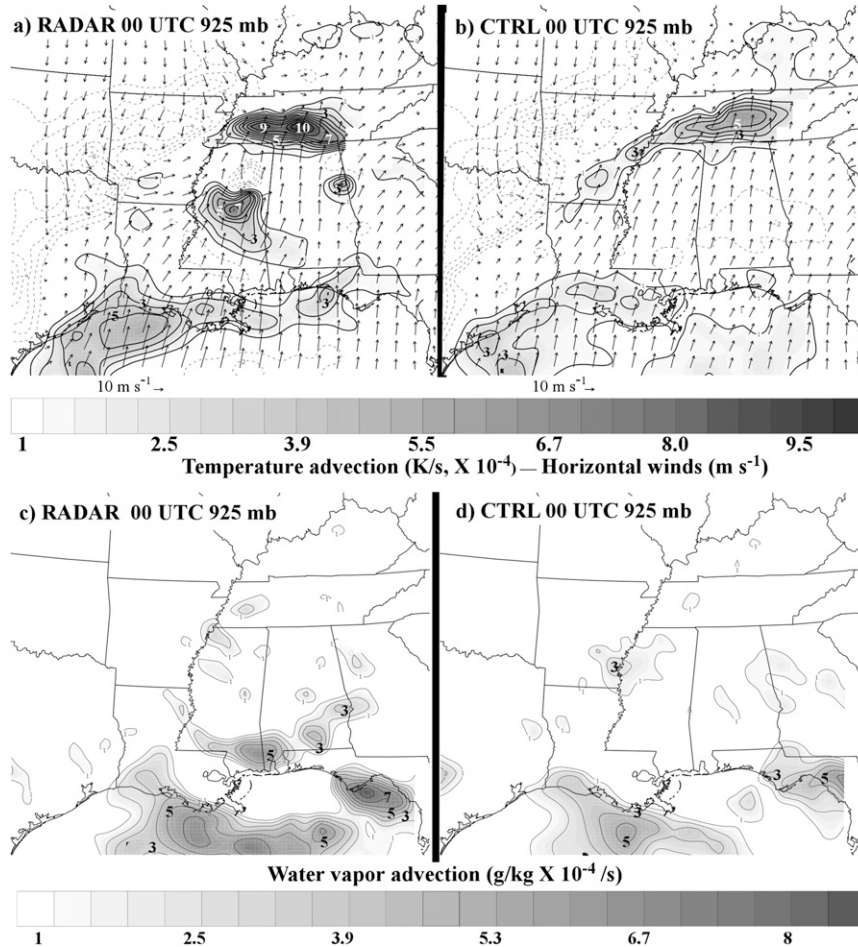


FIG. 17. Temperature and water vapor advection at 0000 UTC 30 Apr 2005.

the western Gulf of Mexico, just off the Texas coast. This flow feature is simulated correctly at the location of a line of low-level cloud formation preceding the formation of the secondary squall line. Larger moisture and warm-air advection at lower atmospheric layers with stronger southerly flow for the RADAR experiment are observed from the beginning of the model simulations to our 0600 forecast hour.

b. Formation of the secondary squall line

As shown earlier (Fig. 4c), secondary convection (what will become the secondary squall line ahead of the primary squall line; see Fig. 4d) began by 0600 UTC over southern Louisiana and Mississippi. RADAR was able to forecast the timing and the location of this secondary CI (Fig. 14c). A 0600 UTC sounding from Slidell, Louisiana (KLIX), portrays a very moist 2-km-deep ABL with significant CAPE (2000 J kg^{-1}) at the time of the CI (Fig. 18). The ABL is capped with a moderate temperature inversion. The hourly KLIX WSR-88D VAD anal-

ysis indicates a persistent south-southwesterly flow of 30–40 kt within the ABL (Fig. 18). The winds above 4 km are westerly at 50–70 kt. The persistent southerly and south-southwesterly flow for the period of 0000–0600 UTC carried significant water vapor and relatively warm air to southern Louisiana and Mississippi.

As discussed earlier, the *GOES-12* IR channel at 0015 UTC (Fig. 3a) shows a relatively cloud-free region ahead of the CF over southern Texas and a cloud shield with relatively warmer cloud-top temperatures over central Texas. Meanwhile, a line of convective clouds forms along a low-level trough as it moves eastward, and is used as a proxy to monitor the trough propagation. The low-level trough propagates faster than the surface CF, catches up to the CF by 0300 UTC (not shown), then moves ahead (east) of the CF (Fig. 19a). The location of the CF was discerned from the Houston/Galveston, Texas, radar (KHGX, labeled H) and is depicted with red dots. WSR-88D Z did not suggest any possible gravity wave or surface convergence passage associated

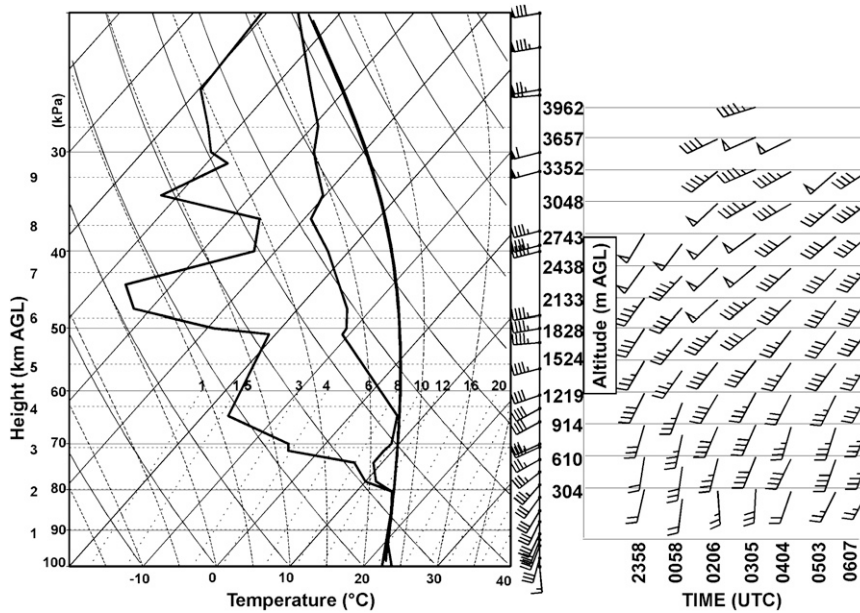


FIG. 18. (left) The 0600 UTC sounding released at Slidell. (right) VAD analysis from 2358 UTC 29 Apr to 0607 UTC 30 Apr 2005.

with the surface CF. The low-level trough at 0545 UTC (Fig. 19b) is located just off the Texas coast and has passed KHGX. Southeasterly flow from the Gulf of Mexico converges with northerly flow along the lower-tropospheric trough line. Surface observations indicate that the CF passage is associated with a 4–5-mb pressure rise and a 6°–8°C (average) temperature drop.

The thermodynamic and kinematic variations associated with the trough passage have a distinctive feature. Over Texas, trough passage was observed by a 2-mb surface pressure increase during the period of 0415–0545 UTC, and a 2°C temperature drop. Some stations also observed wind speed increases from 5 to 8–10 m s^{-1} . Over the Gulf of Mexico, as the trough propagated toward the east, buoy stations experienced only a shift in wind direction, while the temperature and pressure remained unchanged (not shown). Figure 19b indicates a new region of convection with cold convective cloud-top temperatures of -40°C or more over southern Louisiana and southern Mississippi. Conventional surface and Doppler radar observations suggest that this secondary convection was independent from the original squall line located to the north and west.

A VAD time series analysis (Fig. 20) from KHGX examines flow properties associated with the trough passage at lower altitudes. Southerly flow over KHGX dominated the ABL until the CF arrived at 0902 UTC (depicted with an arrow). As the cloud band associated with the trough passes KHGX, the wind direction begins to turn clockwise at about 2-km altitude (depicted with

the shaded region). The ABL flow beneath this level is undisturbed (i.e., southwesterly direction of the flow prior to, and during, trough passage). The wind at 2 km AGL becomes more northerly, then more easterly with time, without affecting the flow beneath.

c. Secondary squall-line development during 0600–0900 UTC

Total precipitable water (PW) at the 0600 UTC forecast hour from RADAR is shown in Fig. 21a. Bands of relatively high PWs (3–4 cm) are collocated with convective clouds associated with the primary squall line (black arrow). The secondary convection, which began 1 h earlier, is implied with deep cloud formation over southern Louisiana (white arrow). The 4–5-cm PW contours over southern and central Louisiana coincide with the formation of new convective clouds. CTRL also captures the location of the primary squall-line clouds, but the secondary convection over southern Louisiana and Mississippi is missed (not shown). Again, this shows the importance of capturing the mesoscale fields properly. The PW differences between the two experiments (Fig. 21b), ranging from 0.25 to 1 cm, depict more PW in the vicinity (ahead of the primary squall line) of the secondary convection region.

Figures 22a and 22b display the water vapor field for the 0600 UTC forecast hour. RADAR predicts greater water vapor content over the western Gulf coast. Typical values of mixing ratios over southern Louisiana were 15–16 g kg^{-1} . CTRL, on the other hand, predicts much

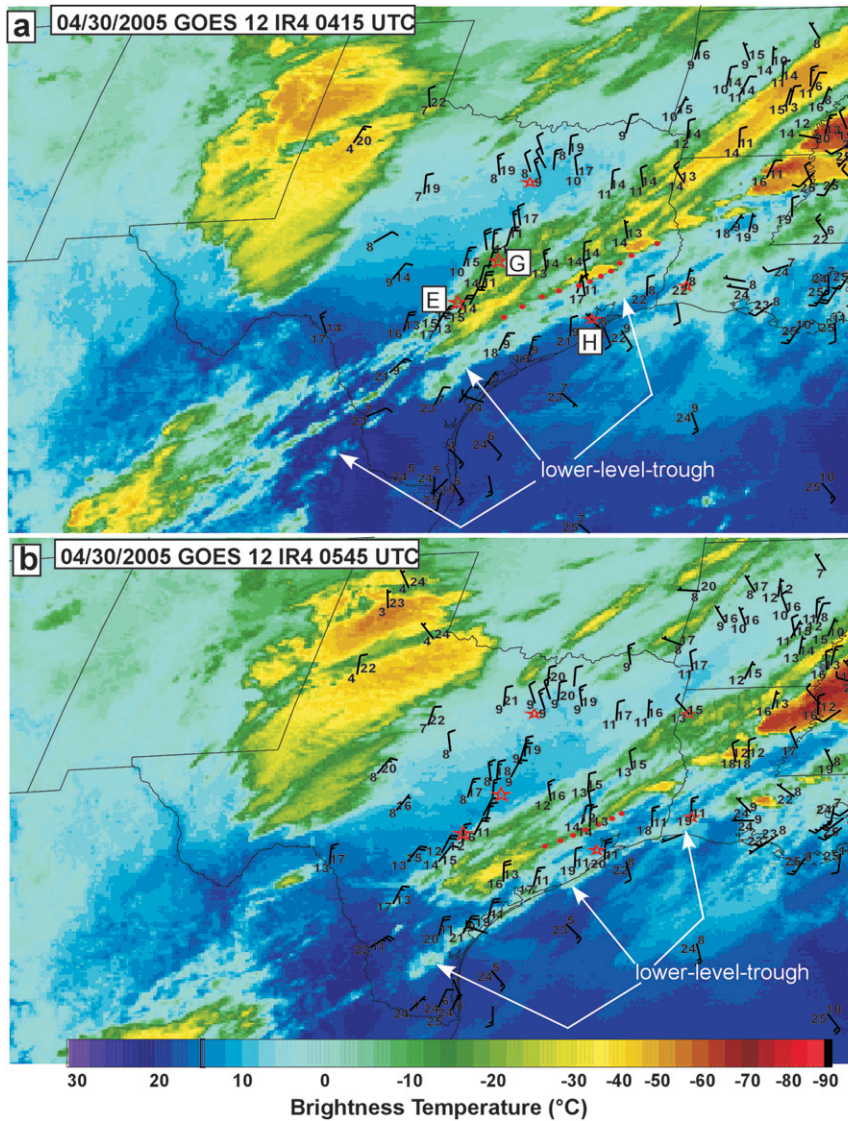


FIG. 19. (a) Brightness temperatures at 0415 UTC 30 Apr 2005 with surface and buoy observations valid at 0500 UTC. The red dots depict the location of the CF observed as a radar fineline delineated by the KHGX radar at 0411 UTC from the lowest elevation angle. The (pressure - 1000) and temperature values are depicted at the upper-right and at the lower-left corners of each of the stations, respectively. Full barbs represent 10-kt winds. (b) Same as in (a) but for the 0545 UTC *GOES-12* IR image and the 0600 UTC surface and buoy observations. KHGX radar at 0544 UTC from the lowest elevation angle was used to locate the fineline associated with the CF. The letters E, G, and H (with stars) depict the locations of the Austin/San Antonio, TX (KEWX); Fort Hood, TX (KGRK), and KHGX Doppler radars. White arrows point to a lower-tropospheric trough.

lower mixing ratios over this region ($\sim 10 \text{ g kg}^{-1}$). The 0600 UTC Slidell sounding (Fig. 18) indicates a 16 g kg^{-1} mixing ratio near the surface. The most unstable air parcels also produce larger CAPE for RADAR. Thus, RADAR yields larger CAPE values due to greater water vapor and warm-air advection at lower levels. The Slidell sounding's CAPE closely agrees with the

RADAR-predicted CAPE. RADAR's Z between 0700 and 0900 UTC portrays the evolution of this secondary squall line (Figs. 22e-g). The secondary squall-line formation from RADAR begins ahead of the primary squall line at about the 0600 forecast hour. RADAR simulations at later hours result in a new squall line that runs parallel to the primary squall line and extends from

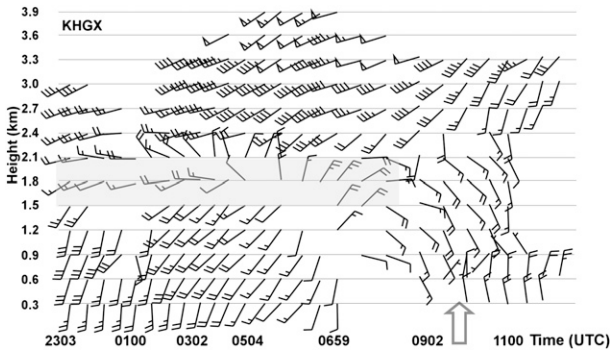


FIG. 20. Time series of VAD acquired from KHGX between 29 and 30 Apr. The shaded region depicts the flow disturbance due to the trough passage. The arrow points to the time of the cold front passage.

southwest Louisiana to central Alabama. By 9 h, RADAR (Figs. 22c and 22g) merges the two squall lines over southern and central Mississippi and Alabama. CTRL forecasted only weak convection over southern Mississippi at the 0900 UTC forecast hour (Fig. 22d). The location and timing of the secondary convection are captured well by RADAR.

5. Conclusions and discussions

A detailed observational and WRF model analysis utilizing WSR-88D radar, surface and upper-air observations, and GOES images shows a chain of events that leads to the formation of two prefrontal squall lines along the western Gulf coast on 29–30 April 2005. The chronological order leading to the first (primary) squall-line formation is 1) an approaching surface CF; 2) its interaction with the ABL, generating an atmospheric bore; 3) propagation of this disturbance along the in-

version layer; and 4) excitation of high-frequency, low-level tropospheric gravity waves initiating convection. The observed AB was 3 times faster than the surface CF. Theoretical calculations of the AB propagation speed and its depth were close to the observed values. This sequence of events manifested itself as low-level convergence ahead of the CF. The kinematics can be detected by WSR-88D radars, and assimilated to improve model prediction of squall-line events. Two WRF model experiments were conducted in which one assimilated conventional observations (CTRL), and another included radar radial winds from nine WSR-88D locations (denoted as RADAR). Better representation of the low-level kinematics in RADAR yielded a distinct convergence line associated with the primary squall line.

The secondary squall line formed in southern Louisiana and Mississippi as the ABL ahead of the primary squall line experienced high water vapor and warm temperature advection from the Gulf of Mexico. A deep dry layer above the ABL, together with the low-level advection, helped to destabilize the atmosphere. Concurrently, a lower-tropospheric trough, propagating faster than the CF, enhanced lifting in the region and instigated the formation of new convection. A 0600 UTC sounding released at Slidell showed that very strong southerly flow had advected more water vapor into the region and created large CAPE values.

The RADAR experiment and observations indicated slow destabilization over the region through advection of colder air aloft, and warm moist air advection at the 850- and 700-mb levels. RADAR was also able to capture the short-wave passage at the 850–700-mb layer. RADAR forecasted the secondary convection not only in the right place but also at about the right time. At the 6-h forecast time, RADAR indicated vertical velocities

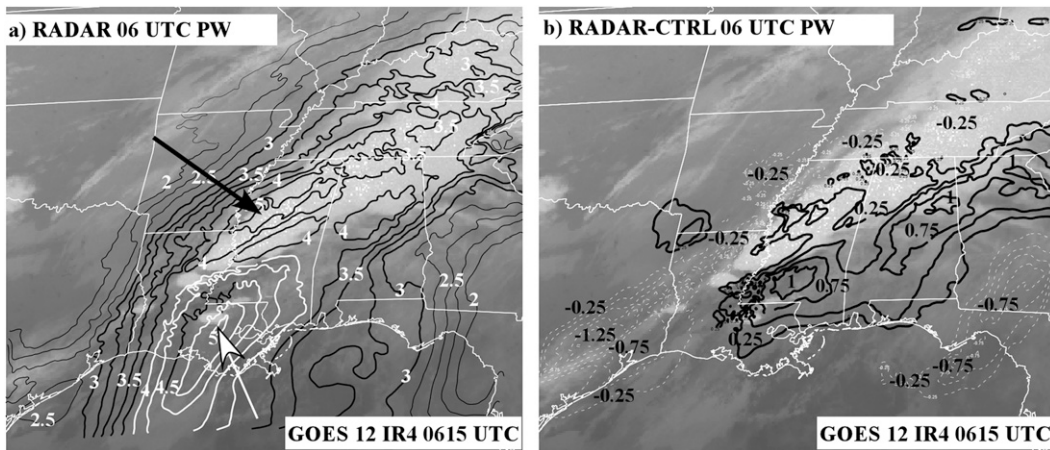


FIG. 21. (a) The 0600 UTC total PW (cm) overlaid on a GOES-12 IR image valid at 0615 UTC 30 Apr 2005. (b) PW differences between the two experiments.

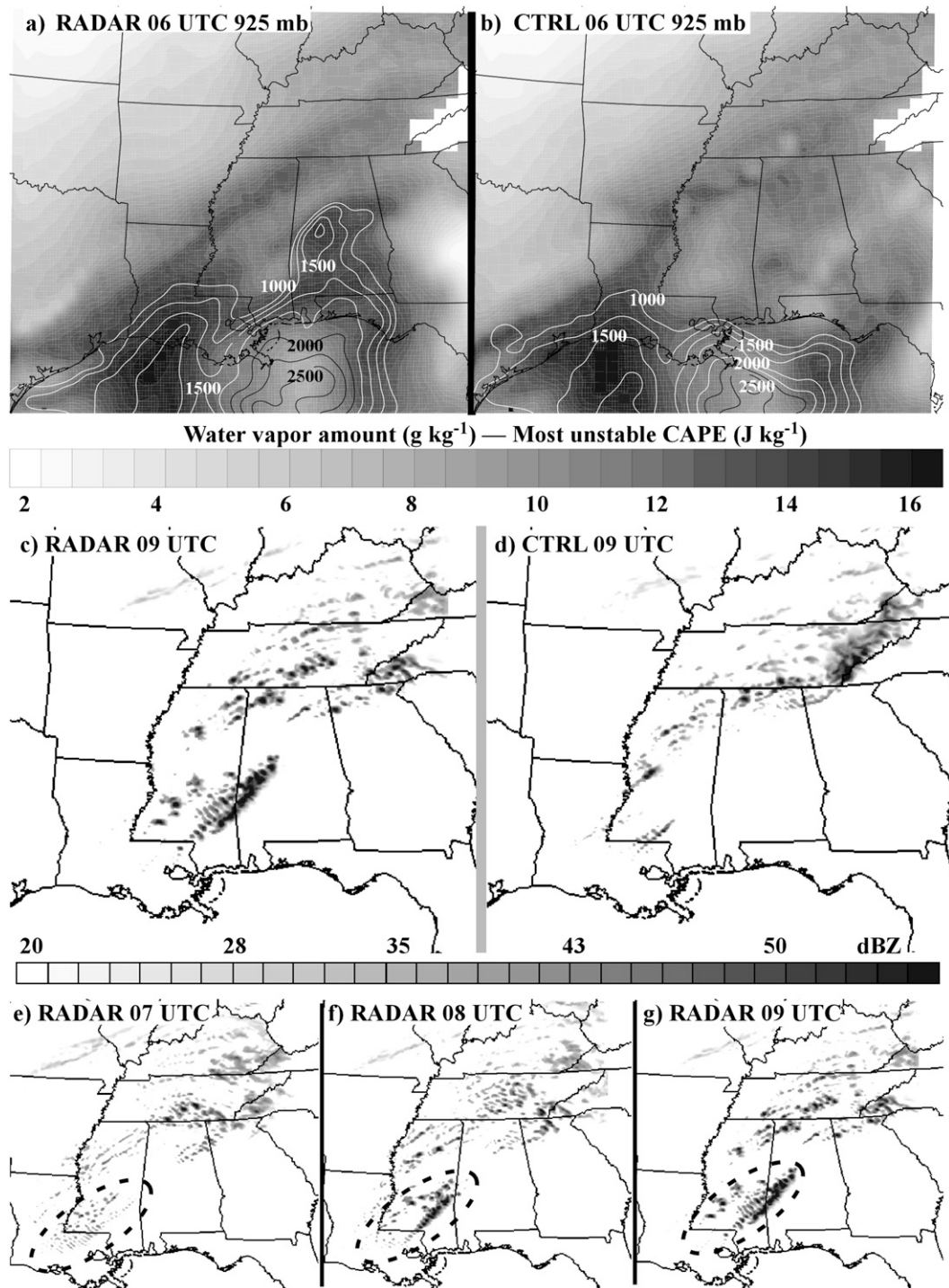


FIG. 22. (a),(b) Water vapor amount (shaded contours) and CAPE for RADAR and CTRL, respectively. Model-produced reflectivity factors for (c) RADAR and (d) CTRL at forecast hour 9. RADAR forecast reflectivity factors are shown for forecast hours (e) 7, (f) 8, and (g) 9. Areas depicted with dashed lines show the region of the secondary squall line.

exceeding 3 m s^{-1} over east-central Louisiana and a small portion of western Mississippi, while CTRL completely missed this secondary convection.

MCSs are composed of multiscale atmospheric interactions. This case showed that CI can be triggered not only by typical along-frontal synoptic or meso- α -scale updrafts, but also by smaller-scale features such as atmospheric bores and lower-tropospheric, high-frequency gravity waves. Determining true atmospheric kinematics, especially within the ABL, is one of the key factors to capturing such small-scale features, and for predicting the timing and location of CI correctly within a 24–48-h forecast.

Acknowledgments. This research was supported by the National Oceanographic and Atmospheric Administration (NOAA) with Grants NA060AR4600181 and NA050AR4601145, and through the Northern Gulf Institute by Grant NA060AR4320264. The SCAN data were provided by the U.S. Department of Agriculture through the National Water and Climate Center. We appreciate the assistance of Niles Oien, an NCAR software engineer, who processed the Doppler radar observations.

REFERENCES

- Atkins, N. T., R. M. Wakimoto, and T. M. Weckwerth, 1995: Observations of the sea-breeze front during CaPE. Part II: Dual-Doppler and aircraft analysis. *Mon. Wea. Rev.*, **123**, 944–969.
- , —, and C. L. Ziegler, 1998: Observations of the finescale structure of a dryline during VORTEX 95. *Mon. Wea. Rev.*, **126**, 525–550.
- Barker, D. M., W. Huang, Y.-R. Guo, A. Bourgeois, and X. N. Xio, 2004: A three-dimensional variational data assimilation system for MM5: Implementation and initial results. *Mon. Wea. Rev.*, **132**, 897–914.
- Benjamin, T. B., 1968: Gravity currents and related phenomena. *J. Fluid Mech.*, **31**, 209–248.
- Christie, D. R., K. J. Muirhead, and A. L. Hales, 1978: On solitary waves in the atmosphere. *J. Atmos. Sci.*, **35**, 805–825.
- Clarke, R. H., R. K. Smith, and D. G. Reid, 1981: The morning glory of the Gulf of Carpentaria: An atmospheric undular bore. *Mon. Wea. Rev.*, **109**, 1726–1750.
- Crook, N. A., 1988: Trapping of low-level internal gravity waves. *J. Atmos. Sci.*, **45**, 1533–1541.
- Dailey, P. S., and R. G. Fovell, 1999: Numerical simulation of the interaction between the sea-breeze front and horizontal convective rolls. Part I: Offshore ambient flow. *Mon. Wea. Rev.*, **127**, 858–878.
- Dorian, P. B., S. E. Koch, and W. C. Skillman, 1988: The relationship between satellite-inferred frontogenesis and squall line formation. *Wea. Forecasting*, **3**, 319–342.
- Doviak, R. J., and R. Ge, 1984: An atmospheric solitary gust observed with a Doppler radar, a tall tower, and a surface network. *J. Atmos. Sci.*, **41**, 2559–2573.
- Dröegemeier, K. K., and R. B. Wilhelmson, 1987: Numerical simulation of thunderstorm outflow dynamics. Part I: Outflow sensitivity experiments and turbulence dynamics. *J. Atmos. Sci.*, **44**, 1180–1210.
- Dudhia, J., 1989: Numerical study of convection observed during the Winter Monsoon Experiment using a mesoscale two-dimensional model. *J. Atmos. Sci.*, **46**, 3077–3107.
- Fovell, R. G., 2005: Convective initiation ahead of the sea-breeze front. *Mon. Wea. Rev.*, **133**, 264–278.
- , G. L. Mullendore, and S.-H. Kim, 2006: Discrete propagation in numerically simulated nocturnal squall lines. *Mon. Wea. Rev.*, **134**, 3735–3752.
- Fulton, R., D. S. Zrnić, and R. J. Doviak, 1990: Initiation of a solitary wave family in the demise of a nocturnal thunderstorm density current. *J. Atmos. Sci.*, **47**, 319–337.
- Hane, C. E., C. L. Ziegler, and H. B. Bluestein, 1993: Investigation of the dryline and convective storms initiated along the dryline: Field experiments during COPS-91. *Bull. Amer. Meteor. Soc.*, **74**, 2133–2145.
- Hong, S.-Y., and Y. Noh, 2006: A new vertical diffusion package with an explicit treatment of entrainment processes. *Mon. Wea. Rev.*, **134**, 2318–2341.
- Hu, M., M. Xue, and K. Brewster, 2006a: 3DVAR and cloud analysis with WSR-88D level-II data for the prediction of the Fort Worth, Texas, tornadic thunderstorms. Part I: Cloud analysis and its impact. *Mon. Wea. Rev.*, **134**, 675–698.
- , —, J. Gao, and K. Brewster, 2006b: 3DVAR and cloud analysis with WSR-88D level-II data for the prediction of the Fort Worth, Texas, tornadic thunderstorms. Part II: Impact of radial velocity analysis via 3DVAR. *Mon. Wea. Rev.*, **134**, 699–721.
- Intrieri, J. M., A. J. Bedard Jr., and R. M. Hardesty, 1990: Details of colliding thunderstorm outflows as observed by Doppler lidar. *J. Atmos. Sci.*, **47**, 1081–1098.
- Karan, H., and K. R. Knupp, 2006: Mobile Integrated Profiler System (MIPS) observations of low-level convergent boundaries during IHOP. *Mon. Wea. Rev.*, **134**, 92–112.
- , and —, 2009: Radar and profiler analysis of colliding boundaries: A case study. *Mon. Wea. Rev.*, **137**, 2203–2222.
- Kingsmill, D. E., and N. A. Crook, 2003: An observational study of atmospheric bore formation from colliding density currents. *Mon. Wea. Rev.*, **131**, 2985–3002.
- Knupp, K. R., 2006: Observational analysis of a gust front to bore to solitary wave transition within an evolving nocturnal boundary layer. *J. Atmos. Sci.*, **63**, 2016–2035.
- Koch, S. E., 1984: The role of an apparent mesoscale frontogenetic circulation in squall line initiation. *Mon. Wea. Rev.*, **112**, 2090–2111.
- , and W. L. Clark, 1999: A nonclassical cold front observed during COPS-91: Frontal structure and the process of severe storm initiation. *J. Atmos. Sci.*, **56**, 2862–2890.
- , P. B. Dorian, R. Ferrare, S. H. Melfi, W. C. Skillman, and D. Whiteman, 1991: Structure of an internal bore and dissipating gravity current as revealed by Raman lidar. *Mon. Wea. Rev.*, **119**, 857–887.
- , F. Zhang, M. L. Kaplan, Y. L. Lin, R. Weglarz, and M. Trexler, 2001: Numerical simulations of a gravity wave event over CCOPE. Part III: The role of a mountain–plains solenoid in the generation of the second wave episode. *Mon. Wea. Rev.*, **129**, 909–933.
- Lac, C., J. P. Lafore, and J. L. Redelsperger, 2002: Role of gravity waves in triggering deep convection during TOGA COARE. *J. Atmos. Sci.*, **59**, 1293–1316.

- Lim, J.-O. J., and S.-Y. Hong, 2005: Effects of bulk ice microphysics on the simulated monsoonal precipitation over East Asia. *J. Geophys. Res.*, **110**, D24201, doi:10.1029/2005JD006166.
- Liu, C.-H., and M. W. Moncrieff, 1996: A numerical study of the effects of ambient flow and shear on density currents. *Mon. Wea. Rev.*, **124**, 2282–2303.
- , and —, 2000: Simulated density currents in idealized stratified environments. *Mon. Wea. Rev.*, **128**, 1420–1437.
- Locatelli, J. D., M. T. Stoelinga, and P. V. Hobbs, 2002: A new look at the super outbreak of tornadoes on 3–4 April 1974. *Mon. Wea. Rev.*, **130**, 1633–1651.
- Mlawer, E. J., S. J. Taubman, P. D. Brown, M. J. Iacono, and S. A. Clough, 1997: Radiative transfer for inhomogeneous atmosphere: RRTM, a validated correlated-*k* model for the long-wave. *J. Geophys. Res.*, **102** (D14), 16 663–16 682.
- Moncrieff, M. W., and C.-H. Liu, 1999: Convection initiation by density currents: Role of convergence, shear, and dynamical organization. *Mon. Wea. Rev.*, **127**, 2455–2464.
- Mueller, C. K., and R. E. Carbone, 1987: Dynamics of a thunderstorm outflow. *J. Atmos. Sci.*, **44**, 1879–1897.
- Parrish, D. F., and J. C. Derber, 1992: The National Meteorological Center's spectral statistical-interpolation analysis system. *Mon. Wea. Rev.*, **120**, 1747–1763.
- Ralph, F. M., C. Mazaudier, M. Crochet, and S. V. Venkateswaran, 1993: Doppler Sodar and radar wind-profiler observations of gravity-wave activity associated with a gravity current. *Mon. Wea. Rev.*, **121**, 444–463.
- Rottman, J. W., and J. E. Simpson, 1989: The formation of internal bores in the atmosphere: A laboratory model. *Quart. J. Roy. Meteor. Soc.*, **115**, 941–963.
- Shapiro, M. A., T. Hampel, D. Rotzoll, and F. Mosher, 1985: The frontal hydraulic head: A micro- α (~ 1 km) triggering mechanism for mesoconvective weather systems. *Mon. Wea. Rev.*, **113**, 1166–1183.
- Simpson, J. E., 1997: *Gravity Currents in the Environment and the Laboratory*. 2nd ed. Cambridge University Press, 244 pp.
- Skamarock, W. C., J. B. Klemp, J. Dudhia, D. O. Gill, D. Barker, W. Wang, and J. G. Powers, 2005: A description of the Advanced Research WRF version 2. NCAR Tech. Note NCAR/TN-468+STR, 88 pp.
- Ulanski, S. L., and M. Garstang, 1978: The role of surface divergence and vorticity in the life cycle of convective rainfall. Part I: Observation and analysis. *J. Atmos. Sci.*, **35**, 1047–1062.
- Wakimoto, R. M., and N. T. Atkins, 1994: Observations of the sea-breeze front during CaPE. Part I: Single-Doppler, satellite, and cloud photogrammetry analysis. *Mon. Wea. Rev.*, **122**, 1092–1114.
- , and D. E. Kingsmill, 1995: Structure of an atmospheric unidular bore generated from colliding boundaries during CaPE. *Mon. Wea. Rev.*, **123**, 1374–1392.
- Weckwerth, T. M., and R. M. Wakimoto, 1992: The initiation and organization of convective cells atop a cold-air outflow boundary. *Mon. Wea. Rev.*, **120**, 2169–2187.
- , T. W. Horst, and J. W. Wilson, 1999: An observational study of the evolution of horizontal convective rolls. *Mon. Wea. Rev.*, **127**, 2160–2179.
- Wilhelmson, R. B., and C. Chen, 1982: A simulation of the development of successive cells along a cold outflow boundary. *J. Atmos. Sci.*, **39**, 1466–1483.
- Wilson, J. W., and W. E. Schreiber, 1986: Initiation of convective storms and radar-observed boundary-layer convergence lines. *Mon. Wea. Rev.*, **114**, 2516–2536.
- , T. M. Weckwerth, J. Vivekanandan, R. M. Wakimoto, and R. W. Russell, 1994: Boundary layer clear-air radar echoes: Origin of echoes and accuracy of derived winds. *J. Atmos. Oceanic Technol.*, **11**, 1184–1206.
- Xiao, Q., Y. H. Kuo, J. Sun, W. C. Lee, E. Lim, Y. R. Guo, and D. M. Barker, 2005: Assimilation of Doppler radar observations with a regional 3DVAR system: Impact of Doppler velocities on forecasting of a heavy rainfall case. *J. Appl. Meteor.*, **44**, 768–788.
- , and Coauthors, 2008: Doppler radar data assimilation in KMA's operational forecasting. *Bull. Amer. Meteor. Soc.*, **89**, 39–43.
- Xu, Q., 1992: Density currents in shear flows—A two-fluid model. *J. Atmos. Sci.*, **49**, 511–524.
- , and M. W. Moncrieff, 1994: Density current circulations in shear flows. *J. Atmos. Sci.*, **51**, 434–446.
- Xue, M., and W. J. Martin, 2006: A high resolution modeling study of the 24 May 2002 dryline case during IHOP. Part II: Horizontal convective rolls and convective initiation. *Mon. Wea. Rev.*, **134**, 172–191.
- , Q. Xu, and K. E. Droegemeier, 1997: A theoretical and numerical study of density currents in sheared environments within a vertically confined channel. *J. Atmos. Sci.*, **54**, 1998–2019.
- Zhao, Q., J. Cook, Q. Xu, and P. R. Harasti, 2006: Using radar wind observations to improve mesoscale numerical weather prediction. *Wea. Forecasting*, **21**, 502–522.
- Ziegler, C. L., W. J. Martin, R. A. Pielke, and R. L. Walko, 1995: A modeling study of the dryline. *J. Atmos. Sci.*, **52**, 263–285.